Unbalanced Frontogenesis. Part I: Zero Potential Vorticity

WILLIAM BLUMEN

Program in Atmospheric and Oceanic Sciences, University of Colorado, Boulder, Colorado

R. T. WILLIAMS

Department of Meteorology, Naval Postgraduate School, Monterey, California

(Manuscript received 14 March 2000, in final form 6 February 2001)

ABSTRACT

Unbalanced frontogenesis is studied in a two-dimensional, Boussinesq, rotating fluid that is constrained between two rigid, level surfaces. The potential vorticity is zero. The initial state is unbalanced because there is no motion and the potential temperature is given by the error function of x. An analytic solution is derived based on the neglect of the barotropic pressure gradient. The solution procedure uses momentum coordinates to obtain nonlinear solutions. When the initial Rossby number (Ro) is less than 1.435 the horizontal wind components display an inertial oscillation. During the first part of the inertial period ($0 < ft < \pi$) the isentropes develop a tilt and frontogenesis occurs, while in the second part ($\pi < ft < 2\pi$) the isentropes return to a vertical orientation and frontolysis brings the temperature gradient back to its original value at $ft = 2\pi$. For larger values of Ro a frontal discontinuity forms before $ft = \pi$.

The importance of the barotropic pressure gradient is determined in a scale collapse problem with a constant potential temperature and no rotation. In this case the inclusion of the barotropic pressure gradient increases the time before the discontinuity forms.

Numerical solutions of the original problem with rotation show that the presence of the barotropic pressure gradient term increases the critical Rossby number from 1.435 to about 1.55. Otherwise the complete solutions are very similar to the analytic solutions, except that the isentropes are no longer straight and the vorticity shows evidence of strong vertical advection by a small-scale vertical jet. Further, shorter timescales are expected with unbalanced fronts as compared with balanced fronts.

1. Introduction

In balanced frontogenesis the vorticity is larger than the divergence and the tangential wind component is nearly geostrophic. The Hoskins and Bretherton (1972) semigeostrophic theory of frontogenesis shows how a frontal zone that begins on the synoptic scale can collapse to a discontinuity in a finite time. Throughout this process the vorticity remains larger than the divergence even though the Rossby number is greater than one. Studies by Gall et al. (1987, 1988) and Snyder et al. (1993) suggest that this relationship between the vorticity and the divergence holds past the time when the semigeostrophic equations fail as long as there is no friction.

In unbalanced frontogenesis the pressure gradient normal to the front is not in geostrophic balance. Usually these conditions arise with smaller-scale circulations where the Rossby number is not small. These situations usually occur in the atmosphere near the surface where there are large horizontal gradients in heating. For example, the sea breeze that arises from the land–sea heating gradient can develop a sea-breeze front (Estoque 1962). In general heating gradients caused during the day between clear and cloudy areas can lead to significant temperature differences (Segal et al. 1986; Segal et al. 1993). When low-level clouds are present behind a cold front, solar heating can induce unbalanced frontogenesis, which can greatly intensify the original cold front (Koch et al. 1995; Blumen et al. 1996). If the original cold front is the result of balanced frontogenesis, this mechanism shows how balanced and unbalanced frontogenesis can work together to produce an intense small-scale front that is embedded in a larger-scale system. Unbalanced frontogenesis can also occur in the ocean where sources and sinks of salinity can be important as well as heating and cooling.

The objective of this two-part study is to investigate unbalanced frontogenesis in its simplest form. We will choose initial conditions that contain unbalanced temperature and wind fields. Heating and friction will be neglected even though heating may be needed to pro-

Corresponding author address: R. T. Williams, Department of Meteorology, Naval Postgraduate School, 589 Dyer Rd., Room 254, Monterey, CA 93943-5114.
E-mail: williart@met.nps.navy.mil

duce the initial state. We will use the Boussinesq equations and the fluid will be confined between two rigid horizontal plates that are normal to gravity. This is an idealization of an atmospheric situation in which a front would develop near the lower boundary.

Various theoretical and laboratory studies show that in the absence of rotation, an initial horizontal density gradient can increase significantly due to advective effects. Simpson and Linden (1989) consider a fluid that is initially at rest with constant vertical and horizontal density gradients. They show that vertically sheared horizontal motion develops in response to the horizontally constant pressure gradient force. The latter varies linearly with height in hydrostatic balance with the uniform horizontal density gradient. The horizontal fluid motion causes the constant density lines to rotate toward the horizontal so that the vertical density gradient increases continually with time while the horizontal density gradient remains constant. In this process no vertical motion develops and the horizontal velocity increases linearly with time. Simpson and Linden also consider an initial state consisting of two regions with constant, but different, density gradients. These regions meet along a vertical line with the density everywhere continuous. They predict the formation of a discontinuity in density within a finite time along one of the horizontal boundaries at the interface between the two regions. The front forms as a result of the convergence between the larger horizontal velocities in the large density gradient region and the smaller horizontal velocities in the small density gradient region. In this case vertical motions develop and the frontal zone tilts so that the denser fluid is underneath it. Simpson and Linden verify the predicted behavior with tank experiments in which the density is varied with the salt concentration. Follow-up studies by Jacqmin (1991) and Kay (1992) investigate the increase in density gradient in fluids with quadratic distributions of density. They show that infinitely large velocities and density gradients will develop along the bottom boundary in the absence of diffusion. This behavior is unrealistic for geophysical applications.

In a rotating regime we expect that the scale collapse described by Simpson and Linden (1989) will be modified or, perhaps, even prevented. Blumen and Wu (1995) and Wu and Blumen (1995) treat this problem in terms of geostrophic adjustment. They use conservation of mass, momentum and potential vorticity to determine a geostrophically balanced state from an initially unbalanced state. They employ the momentum coordinates (Hoskins and Bretherton 1972), but they do not use the semigeostrophic approximation. The amount of frontogenesis in each case is determined by examining the final state that is in geostrophic balance. In particular it is assumed that frontogenesis has occurred if a nonsingular fluid state cannot be found.

Blumen (2000) obtains analytic solutions to the unbalanced initial value problem for the case of zero potential vorticity. Following Blumen and Wu (1995) the equations for conservation of mass, momentum, and potential vorticity are transformed into the momentum coordinates. The velocity is separated into geostrophic and ageostrophic parts and new variables defined by following Hoskins and Draghici (1977) are introduced. The initial state is at rest with temperature as a function of x. An inertial oscillation is obtained in the transformed coordinates, with the Coriolis frequency f. In physical coordinates the solution is the sum of an inertial oscillation and an evolving geostrophic flow. The behavior of the solution depends on the initial Rossby number Ro. When Ro is less than a critical value, the temperature gradient increases (frontogenesis) during the half-period $0 < t < \pi/f$ and the gradient decreases (frontolysis) during the second half-period $\pi/f < t \leq 2\pi/f$. When Ro is greater than the critical value, a discontinuity forms at the top and bottom boundaries during $0 < t < \pi/f$. In order to obtain analytic time-dependent solutions Blumen (2000) neglects the barotropic part of the pressure gradient.

In this paper, Part I, we will evaluate the effect of the neglect of the barotropic pressure gradient by comparing the analytic solutions with numerical solutions of the full time-dependent equations. The Part II of this study will consider the case of uniform potential vorticity.

In section 2 the Boussinesq equations are developed with appropriate scaling. An approximate solution is developed in section 3, and emphasis is placed on the top and bottom boundaries. The numerical model, used in the study, is described in section 4. Special solutions are given in section 5, which isolate the effects of the barotropic pressure gradient term. The numerical solutions for zero potential vorticity are presented in section 6 and compared with the analytic solutions from section 3. The conclusions are found in section 7.

2. Model

The present model is a time-dependent version of the model used by Ou (1984) and Blumen and Wu (1995) to derive steady geostrophic flows that evolve from an initial mass imbalance. The initial-value problem is bypassed in these investigations; here it is developed. The fluid is Boussinesq and inviscid; the constant rotation rate is $f/2$, where f is the Coriolis parameter, and the motion is constrained to the (x, z) plane, where x is horizontally directed and z is directed upward antiparallel to gravity g. The fluid is assumed to be unbounded in $|x|$, with rigid, level surfaces at $z = 0,h$.

The basic equations of this Boussinesq model are

$$\frac{\partial u}{\partial t} + u\frac{\partial u}{\partial x} + w\frac{\partial u}{\partial z} - fv = -\frac{\partial \pi}{\partial x}, \tag{2.1}$$

$$\frac{\partial v}{\partial t} + u\frac{\partial v}{\partial x} + w\frac{\partial v}{\partial z} + fu = 0, \tag{2.2}$$

$$0 = -\frac{\partial \pi}{\partial z} + \frac{\theta g}{\theta(0)}, \tag{2.3}$$

$$\frac{\partial u}{\partial x} + \frac{\partial w}{\partial z} = 0, \tag{2.4}$$

$$\frac{\partial \theta}{\partial t} + u\frac{\partial \theta}{\partial x} + w\frac{\partial \theta}{\partial z} = 0. \tag{2.5}$$

Here (u, w) are velocity components in the (x, z) directions; v is directed normal to the (x, z) plane; $\pi = p/\rho(0)$, where p denotes the pressure; $\rho(0)$ is a reference density; and the temperature anomaly is defined as

$$\theta = [\theta_{\text{tot}} - \theta(0)], \tag{2.6}$$

where θ_{tot} is the temperature and $\theta(0)$ is a reference temperature. The density anomaly used by Ou (1984) and Blumen and Wu (1995) is $\rho = -\theta$, under the Boussinesq approximation.

These equations are cast into nondimensional form by introduction of

$$\begin{aligned} x &= \lambda x', \qquad z = hz', \qquad t = f^{-1}t', \\ (u, v) &= (g^*h)^{1/2}(u', v'), \qquad w = \lambda^{-1}h(g^*h)^{1/2}w', \\ \pi &= f\lambda(g^*h)^{1/2}\pi', \qquad \theta = \Delta\theta\theta'. \end{aligned} \tag{2.7}$$

The internal deformation radius is $\lambda = (g^*h)^{1/2}f^{-1}$, where $g^* = g\Delta\theta/\theta(0)$ denotes reduced gravity and $\Delta\theta$ is the magnitude of the initial temperature anomaly. The set of equations (2.1)–(2.5) may be expressed as

$$\frac{\partial u}{\partial t} + u\frac{\partial u}{\partial x} + w\frac{\partial u}{\partial z} - v = -\frac{\partial \pi}{\partial x}, \tag{2.8}$$

$$\frac{\partial v}{\partial t} + u\frac{\partial v}{\partial x} + w\frac{\partial v}{\partial z} + u = 0, \tag{2.9}$$

$$0 = -\frac{\partial \pi}{\partial z} + \theta, \tag{2.10}$$

$$\frac{\partial u}{\partial x} + \frac{\partial w}{\partial z} = 0, \tag{2.11}$$

$$\frac{\partial \theta}{\partial t} + u\frac{\partial \theta}{\partial x} + w\frac{\partial \theta}{\partial z} = 0, \tag{2.12}$$

where the prime notation in (2.7) has been dropped.

The boundary conditions are

$$\begin{aligned} w &= 0, \qquad z = 0, 1, \\ u, v &\to 0 \qquad \text{as } |x| \to \infty, \\ \frac{\partial \theta}{\partial x} &\to 0 \qquad \text{as } |x| \to \infty. \end{aligned} \tag{2.13}$$

The initial state is one of rest ($u = v = w = 0$) and the temperature anomaly (2.6) is represented in nondimensional variables by

$$\theta = \theta_0(x_0), \qquad t = 0, \tag{2.14}$$

where the temperature anomaly θ_0 is only a function of the horizontal coordinate $x = x_0$. The reason for the notation x_0, to denote the initial position, will become apparent later. This flow has zero potential vorticity, which holds for all time. The distinction between these flow regimes is presented more fully by Blumen and Wu (1995).

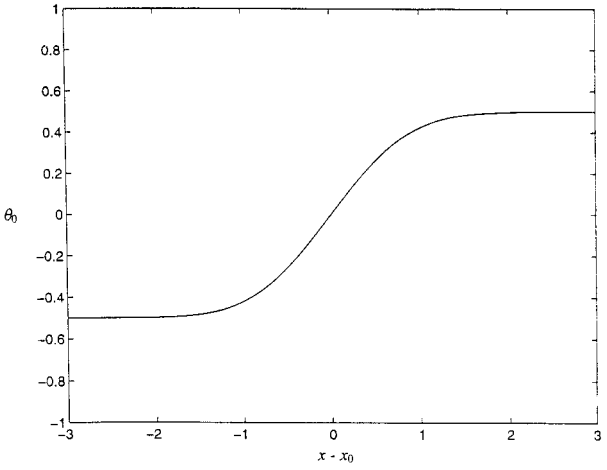

FIG. 1. The initial potential temperature θ_0 as a function of x.

The mass imbalance represented by a temperature anomaly will initiate motion: the adaptation toward a steady-state thermal wind balance. This process will be examined by specification of the antisymmetric distribution used by Blumen and Wu and represented by

$$\theta_0(x_0) = \frac{1}{2}\,\text{erf}(ax_0) = \frac{1}{\pi^{1/2}}\int_0^{ax_0} e^{-t^2}\,dt, \tag{2.15}$$

where erf denotes the error function. This initial state differs from the sinusoidal initial state that is used by Blumen (2000). The nondimensional inverse scale a may be interpreted as a Rossby number

$$a = \frac{(g^*h)^{1/2}}{fL}, \tag{2.16}$$

based on velocity $(gh\Delta\theta/\theta(0))^{1/2}$ and length scale L associated with the initial temperature anomaly. The range of θ_0 in (2.15) is unity, so that $\Delta\theta$ represents the total horizontal temperature change in the initial state. This temperature distribution is displayed in Fig. 1.

3. Theory

An analytic development is given in Blumen (2000). In this section we derive the solutions on the upper and lower boundaries, where discontinuities first occur. The development proceeds by use of momentum coordinates, which may be exploited to yield a relatively simple mathematical problem. Briefly these coordinates are expressed as

$$X = x + v, \qquad Z = z, \qquad T = t, \tag{3.1}$$

and, in view of (2.9), X is conserved so that

$$X = x_0 \tag{3.2}$$

since $v_0(x_0) = 0$. An isotherm at position x_0 in the initial

state will be found at position $x = x_0 - v(x_0, z, t)$ at a given level z and time t.

Thermal wind balance is represented by

$$\frac{\partial v_g}{\partial Z} = \frac{\partial \theta}{\partial X} = \frac{\partial \theta_0}{\partial x_0}. \tag{3.3}$$

The solution for the geostrophic flow $v_g(X, Z)$ from (14) in Blumen and Wu,

$$v_g = -\frac{\partial \theta_0}{\partial x_0}\left(\frac{1}{2} - Z\right), \tag{3.4}$$

where $\theta_0 = -\rho_0$, is also used in this analytic solution. This equation neglects the vertical mean v_g, which is equal to the vertical mean pressure gradient. The dimensional expression for the vertical mean or barotropic pressure gradient is given by (4.2). The effects of the neglect of this term will be isolated in section 5. The full numerical solutions in section 6 are in general agreement with the analytic theory with some modifications.

Equations (2.8) and (2.9) may now be expressed as

$$\frac{\partial u}{\partial t} + u\frac{\partial u}{\partial x} + w\frac{\partial u}{\partial z} - v' = 0, \tag{3.5}$$

$$\frac{\partial v'}{\partial t} + u\frac{\partial v}{\partial x} + w\frac{\partial v}{\partial z} + u = 0, \tag{3.6}$$

where the ageostrophic velocity is $v'(x, z, t)$. Transformation to momentum coordinates yields

$$\frac{\partial u}{\partial T} + u\frac{\partial u}{\partial X} + w\frac{\partial u}{\partial Z} - v' + \frac{\partial u}{\partial X}\left(\frac{\partial v'}{\partial t} + u\frac{\partial v}{\partial x} + w\frac{\partial v}{\partial z}\right) = 0. \tag{3.7}$$

Introduction of (3.6) into (3.7) yields

$$\frac{\partial u}{\partial T} + w\frac{\partial u}{\partial Z} - v' = 0. \tag{3.8}$$

Similarly, (3.6) is transformed into

$$\frac{\partial v'}{\partial T} + w\frac{\partial v}{\partial Z} + u = 0. \tag{3.9}$$

Equations (3.8) and (3.9) may be readily solved on a level boundary, where $w = 0$. The solution for v' is

$$v' = A(X)\sin T + B(X)\cos T, \tag{3.10}$$

where $A(X)$ and $B(X)$ are to be determined. The initial conditions are $v = 0$ and $u = 0$. Consequently, the initial conditions on the upper or lower boundary are

$$v'(X) = -v_g(X),$$
$$\partial v'(X)/\partial T = -u = 0, \qquad T = 0 \tag{3.11}$$

and (3.10) becomes

$$v' = -v_g \cos T. \tag{3.12}$$

The full solutions on the boundaries are

$$v = v_g(1 - \cos T), \tag{3.13}$$

$$u = -v_g \sin T. \tag{3.14}$$

These solutions demonstrate that inertial motion is superposed on a stationary geostrophic flow.

The condition for the frontal formation is given by (9a) in Blumen and Wu,

$$1 - \frac{\partial v}{\partial X} = 0, \tag{3.15}$$

which expresses the condition for a zero-order discontinuity to occur, expressed as the relative vorticity becoming infinite, $\partial v/\partial x = \infty$. Insertion of (3.13) into (3.15) yields

$$1 - \frac{\partial v_g}{\partial X}(1 - \cos T) = 0. \tag{3.16}$$

At the lower boundary substitution from (3.4) with $Z = 0$ into (3.16) gives

$$(1 - \cos T)\frac{\partial^2 \theta_0}{\partial x_0^2} = -2, \tag{3.17}$$

where $\partial/\partial X = \partial/\partial x_0$.

The critical time $T = t_c$ for a front to form may be determined from (3.17) as

$$1 - \cos t_c = 2\Big/\left(-\frac{\partial^2 \theta_0}{\partial x_0^2}\right)_{\max}, \qquad Z = 0, \tag{3.18}$$

where $(-\partial^2\theta_0/\partial x_0^2)_{\max} > 0$ determines t_c. The frontal position is then found by means of $x = x_0 - v(x_0, 0, t_c)$. At the top where $Z = 1$ the critical time can be obtained from

$$1 - \cos t_c = 2\Big/\left(\frac{\partial^2 \theta_0}{\partial x_0^2}\right)_{\max}, \qquad Z = 1. \tag{3.19}$$

In this study the front will form at the same time on both boundaries because the initial temperature is antisymmetric. If this is not the case the fronts will form at different times on the two boundaries, but the solution breaks down when the discontinuity first appears.

For the initial temperature distribution given by (2.15) the condition for frontal formation (3.18) becomes

$$1 - \cos t_c = \frac{(2\pi e)^{1/2}}{\mathrm{Ro}^2}. \tag{3.20}$$

The Blumen and Wu (1995) critical value for the stationary flow to have a zero-order discontinuity is obtained by removing the $\cos t_c$ term in (3.20):

$$\mathrm{Ro} = a = (2\pi e)^{1/4} = 2.03.$$

Inspection of (3.20) shows that values ($a > a_c$) are required for frontal formation. The critical value $a_c = (2\pi e)^{1/4}/2^{1/2} = 1.435$ is associated with one-half an inertial period, $T = \pi e$. Values $a < a_c$ will not produce fronts, but the temperature and geostrophic velocity gra-

dients will be modulated by an inertial oscillation undergoing alternately frontogenesis and frontolysis.

Blumen (2000) finds a critical Rossby number of $a_c = 1$ with the sinsoidal initial temperature field. This is very similar to the value 1.435, which we find for the error function initial temperature field considering the flexibility in defining the Rossby number. Blumen derives the interior solution for u, v, w, and θ, but omits the barotropic pressure field. In particular the isotherms are always straight lines in the x-z plane. Verification of the analytic solutions will be sought in section 6 from the numerical integrations of (2.8)–(2.12) using the initial state represented by (2.15).

4. Numerical model

The equations (2.1)–(2.5) are solved with the same finite differences as used by Williams et al. (1992) although the topographic terms are not needed in the present study. The grid points are staggered in x so the temperature and pressure points lie between the horizontal velocity points, and in z so that the vertical velocity points are between the points that carry the other variables. The nonlinear terms are formulated to conserve the domain average of square quantities so that the sum of kinetic and potential energy will be conserved. Euler backward time differencing is used. There is no heating or friction except for dry convective adjustment.

Equation (2.1) is solved by separating the pressure gradient into vertical mean ($\overline{\ }$) and departure ( )* terms:

$$\frac{\partial \pi}{\partial x} = \left(\overline{\frac{\partial \pi}{\partial x}}\right) + \left(\frac{\partial \pi}{\partial x}\right)^*. \tag{4.1}$$

The departure term is computed by integrating the hydrostatic equation (2.3) and then setting the vertical mean to zero. The barotropic pressure gradient term

$$\left(\overline{\frac{\partial \pi}{\partial x}}\right) = -\frac{\partial}{\partial x}(\overline{u^2}) + f\overline{v} \tag{4.2}$$

is obtained by taking the vertical mean of (2.1) and by using the condition

$$\overline{\frac{\partial u}{\partial x}} = 0. \tag{4.3}$$

This condition is obtained by averaging (2.4) and using the upper and lower boundary conditions on w.

The barotropic pressure gradient is neglected in the analytic theory in section 3, while the numerical solutions in section 6 include this term. The effects of the barotropic pressure gradient term are isolated in section 5. It will turn out that the effect of the term is significant, but the basic behavior is still described by analytic solutions in section 3.

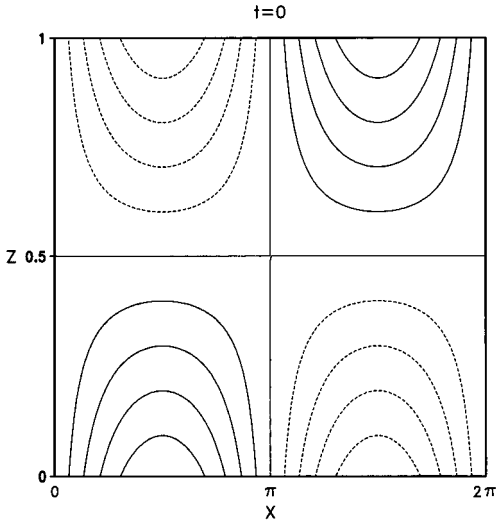

FIG. 2. The initial u field from Eq. (5.3).

5. Role of the barotropic pressure gradient in scale collapse

In order to isolate the role of the barotropic pressure gradient, which is neglected in the theory presented in section 3, we set $f = 0$ and $\theta = 0$ to simplify the equations. The latter condition implies that the potential temperature has the uniform value $\theta(0)$. The nondimensional equation of motion becomes

$$\frac{\partial u}{\partial t} + u\frac{\partial u}{\partial x} + w\frac{\partial u}{\partial z} + \frac{\partial \pi}{\partial x} = 0, \tag{5.1}$$

where u is scaled by its initial amplitude u_o and the timescale is L/u_o. Since $\theta = 0$, the pressure gradient contains only a barotropic component and (4.1) and (4.2) give

$$\frac{\partial \pi}{\partial x} = \overline{\frac{\partial \pi}{\partial x}} = -\frac{\partial}{\partial x}(\overline{u^2}). \tag{5.2}$$

The initial condition is

$$u(x, z, 0) = 2(1/2 - z)\sin x. \tag{5.3}$$

We investigate the scale collapse with these initial conditions by combining (5.1) and (5.2) and by differentiating with respect to x as follows:

$$\frac{\partial}{\partial t}\left(\frac{\partial u}{\partial x}\right) + u\frac{\partial^2 u}{\partial x^2} + \left(\frac{\partial u}{\partial x}\right)^2 + w\frac{\partial^2 u}{\partial x \partial z} + \frac{\partial w}{\partial x}\frac{\partial u}{\partial z} - \frac{\partial^2}{\partial x^2}(\overline{u^2}) = 0.$$

We apply this equation along the symmetry line $x = \pi$ (see Fig. 2) where $u = 0$:

$$\frac{\partial}{\partial t}\left(\frac{\partial u}{\partial x}\right) + \left(\frac{\partial u}{\partial x}\right)^2 + w\frac{\partial^2 u}{\partial x \partial z} - \frac{\partial^2}{\partial x^2}(\overline{u^2}) = 0. \tag{5.4}$$

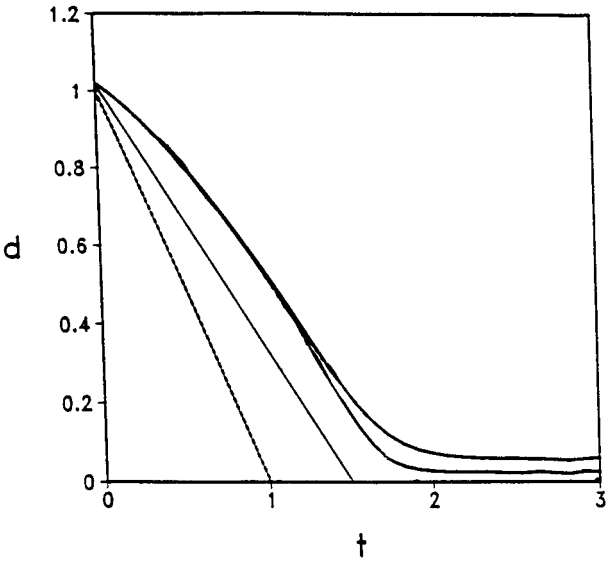

FIG. 3. This graph gives $d = [(\partial u/\partial x)_{\max}]^{-1}$ at $z = 0$ as a function of t. The two solid curves are from the numerical model. The upper and lower curves have grid sizes of $2\pi/157$ and $2\pi/314$, respectively. The other curves are from the indicated equations: (5.6), beaded; (5.15), straight, solid.

We can obtain the solution with no barotropic pressure gradient by applying (5.4) at $z = 0$ where $w = 0$ and neglecting the last term:

$$\frac{\partial}{\partial t}\left(\frac{\partial u}{\partial x}\right) = -\left(\frac{\partial u}{\partial x}\right)^2. \tag{5.5}$$

The solution to this equation is subject to an initial divergence of -1 and is given by

$$\left(\frac{\partial u}{\partial x}\right)^{-1} = -(1 - t). \tag{5.6}$$

This equation shows that a discontinuity forms at $t = 1$. Equation (5.6) is in fact the solution to the inviscid Burgers equation based on the surface u field.

Figure 3 shows a plot of $d = 1/|\partial u/\partial x|_{\max}$ as a function of time t at $z = 0$ for two numerical integrations of the full model. Solution NM2 has one-half the grid size of NM1 and its limiting value of d is about one-half the corresponding value for NM1. This is consistent because the minimum value of d is Δx. Extrapolation from the numerical solution suggests that $d \to 0$ at about $t = 1.75$. The magnitude of the solution (5.6) is also included in the figure. Clearly the neglect of the barotropic pressure gradient term leads to a much earlier discontinuity formation.

It is possible to derive an analytic approximation to the complete solution. Introduce

$$D = \frac{\partial u}{\partial x}$$

into (5.4) and apply it at the upper and lower boundary:

$$\frac{dD}{dt} = -D^2 + \frac{\partial^2}{\partial x^2}(\overline{u^2}) \qquad z = 0, 1. \tag{5.7}$$

In order to estimate the last term in (5.7), we neglect the vertical advection in (5.4) and take the vertical average of the equation, which leads to

$$\frac{\partial^2}{\partial x^2}(\overline{u^2}) = \overline{D^2}, \tag{5.8}$$

where we have used the requirement that $\overline{u} = 0$. Let us assume that D varies linearly between the boundaries. This is true initially [see (5.3)] and the variation in z is at least monotonic throughout the evolution. The divergence can now be written

$$D = \frac{1}{2}(D_T + D_B) + (D_T - D_B)\left(z - \frac{1}{2}\right), \tag{5.9}$$

where D_T and D_B are the values at $z = 1, 0$, respectively. With the symmetry condition and (5.9), the barotropic pressure gradient term can be written after integration:

$$\frac{\partial^2 \overline{u^2}}{\partial x^2} + \overline{D^2} = \frac{1}{3}(D_T^2 + D_B^2 + D_T D_B). \tag{5.10}$$

The initial conditions are

$$D_T(0) = -D_B(0) = 1. \tag{5.11}$$

Based in part on the sign change, let us define

$$D_T = \frac{1}{d_T}, \qquad D_B = -\frac{1}{d_B}. \tag{5.12}$$

Now substitute (5.10) and (5.12) into (5.7) for $z = 0$:

$$\dot{d}_B = -\frac{2}{3} + \left[\left(\frac{d_B}{d_T}\right)^2 - \frac{d_B}{d_T}\right]. \tag{5.13}$$

Here the dot indicates a time derivative; a similar equation d_t is obtained with the opposite sign on the rhs.

Since the bracketed terms in (5.13) cancel initially, a reasonable approximation is as follows:

$$\dot{d}_B = -2/3. \tag{5.14}$$

The solution subject to the initial condition in (5.11) is

$$d_B = 1 - 2/3t. \tag{5.15}$$

This curve is included in Fig. 3 and it shows the formation of a discontinuity at $t = 1.5$. This is within 15% of the value suggested by the numerical solutions. The early time evolution of d_t (not shown) shows growth, but it actually decreases for $t > 0.6$.

Figure 4 contains the u field at $t = 1.5$ and it shows that the vertical variation is no longer linear as in Fig. 2. Apparently the assumption of linear dependence in Eq. (5.9) that is used to derive (5.10) is not too significant. The figure shows that the smallest-scale region is at $x = \pi$ at the bottom. Directly above this point at the

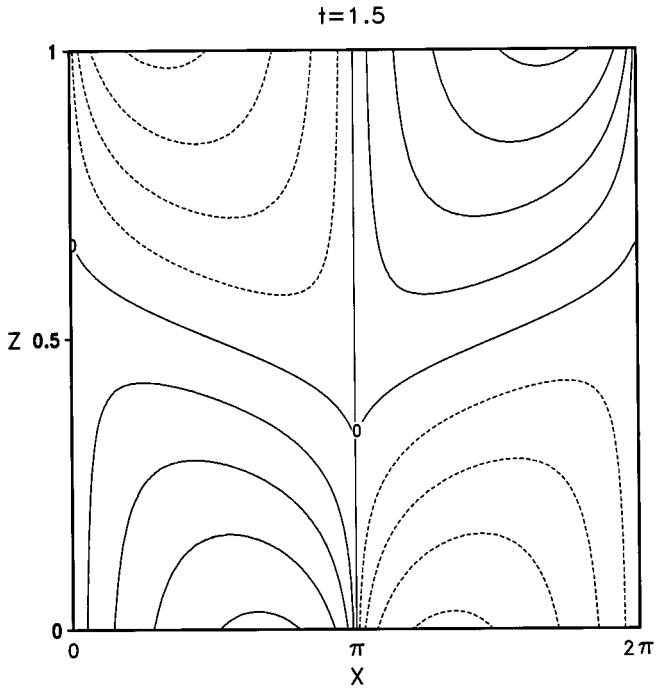

FIG. 4. The numerical solution for u at $t = 1.5$.

top, the scale is less than its initial value (see Fig. 2), even though the extreme values at the top are moving apart.

This analysis shows that the barotropic pressure gradient can be expected to oppose the formation of discontinuities on boundaries, although it can lead to scale reductions at other levels. In the next section it will be shown that when there is strong forcing from a temperature imbalance the barotropic pressure gradient has a much smaller effect.

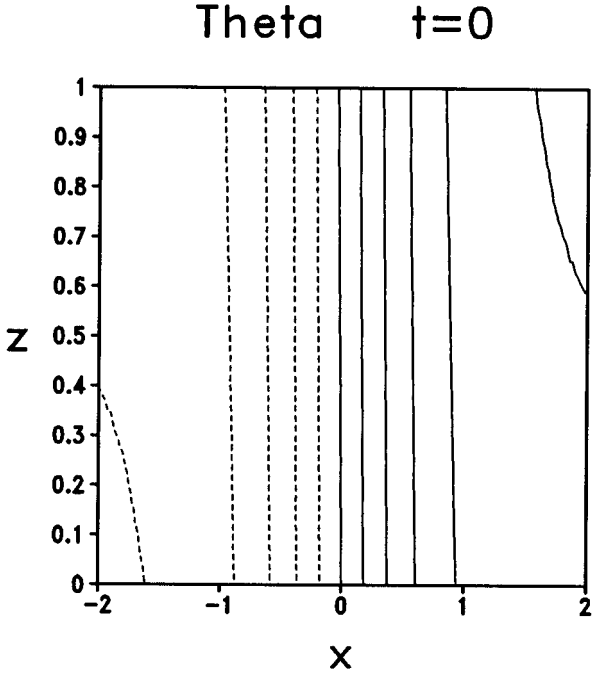

FIG. 5. The initial theta field scaled by $\Delta\theta$. The contour interval is 0.1.

6. Numerical solutions

The initial potential temperature field, for the zero potential vorticity numerical integrations is given in Fig. 5. The field is scaled by $\Delta\theta$ so that θ varies from 0.5 on the right to -0.5 on the left. The x axis is scaled by L, which is the initial frontal scale. In the outer regions (not shown) the θ field contains a reversal of the form of (2.16) to satisfy the periodic boundary conditions. This temperature field is rendered independent of time by including a geostrophic v component in this region. This region is not included in any of the figures and the domain size is always kept large enough that the interior solutions are independent of the boundary region. The numerical experiments also include a very weak stratification that improves the quality of the numerical solutions.

The Rossby number of the first numerical experiment is 1.3, which is below the critical value $a_c = 1.435$. The nondimensional grid increments are $\Delta z = 1/50$ and $\Delta x = 1/50$. The theory of section 3 indicates that an inertial oscillation should be expected with the frontal zone tilting and intensifying and then returning to its initial form. Figure 6 contains θ, w, vorticity and divergence cross sections at $ft = \pi/2$. Dashed lines indicate neg-

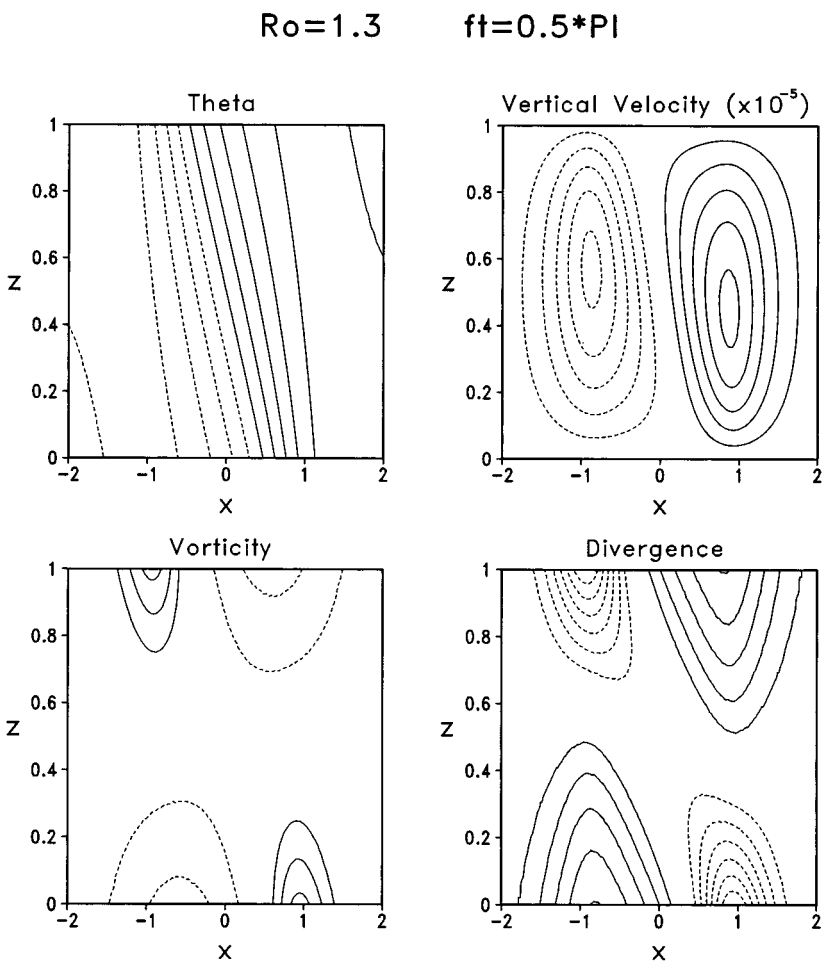

FIG. 6. For Ro = 1.3, the various fields at $ft = \pi/2$. The dimensional fields are obtained by multiplying θ by $\Delta\theta$, w by hf, and ζ and D by multiplying by $[gh\Delta\theta/\theta(\mathrm{o})]^{1/2}/L$, respectively. The contour intervals are θ, 0.2; w, 10^{-5}; ζ, 0.1; D, 0.05. The zero isoline is not included for w, ζ, and D.

ative values. All quantities in this section are scaled as (2.7) unless otherwise indicated. At this time the temperature field begins to tilt with the colder air replacing the warm at the lower boundary and vice versa at the top. This occurs because the u component begins to flow toward low pressure (i.e., toward the cold air at the bottom and warm air at the top). The divergence field in the figure is consistent with this pattern, and it causes the frontogenesis. The vorticity field at this time is growing rapidly and the Coriolis force brings the v field closer to the geostrophic wind. The w field shows a maximum rising motion over the surface frontal position and maximum sinking below the upper front.

Figure 7 contains the same fields as Fig. 6 at $ft = \pi$. The temperature field has increased tilt and increased temperature gradient. At this time the divergence field is very weak except for two convergence regions associated with the surface frontal and upper frontal positions. In the analytic solution the divergence is zero at this time. The vorticity is now much larger than at $ft = \pi/2$, with a large asymmetry between the cyclonic and anticyclonic regions. The maximum values of the vorticity have increased by almost five times and they are associated with the areas of large convergence. This relation is expected since the vorticity is growing due to vertical stretching. The vertical velocity is very weak and the rising and sinking currents are very narrow as expected from the divergence field. However, the vertical advection caused by these narrow jets can be seen in the vorticity field.

The various fields at $ft = 3\pi/2$ are given in Fig. 8. The temperature field is similar to the temperature at $ft = \pi/2$, but the isotherms are tilted more near the boundaries. The divergence field generally resembles the divergence at $ft = \pi/2$ with the signs reversed. However, the divergence contains some smaller-scale features that were not present at $ft = \pi/2$. These seem to be related to the small-scale features present at $ft = \pi$. The vorticity is similar to the $ft = \pi/2$ vorticity, but again smaller-scale features are present with larger extreme

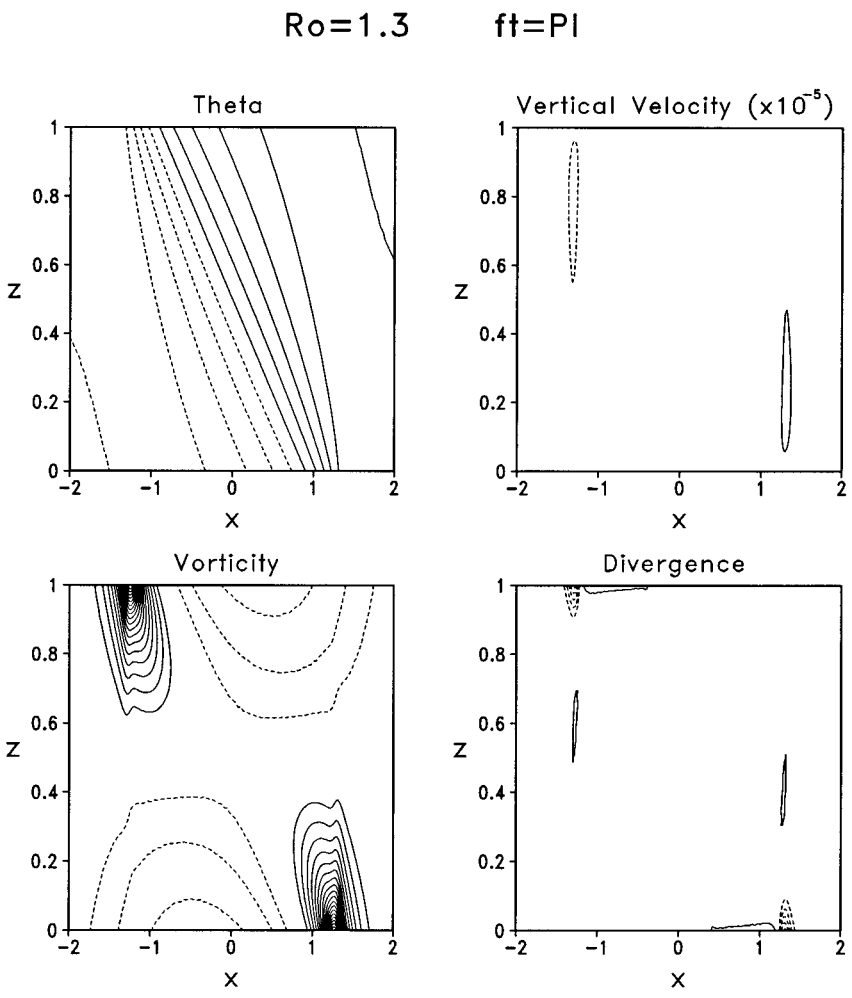

FIG. 7. For Ro = 1.3, the same fields and contour intervals as Fig. 6 but at $ft = \pi$. The extreme values of ζ and D are (2.04, −0.334) and (0.08, −0.32), respectively.

values. The vertical motion field is nearly the reverse of the field at $ft = \pi/2$, except for a small-scale feature that corresponds to similar features in the vorticity and divergence fields. In the analytic theory the temperature and vorticity are the same as at $ft = \pi/2$, and the divergence and vertical motion are reversed.

Figure 9 contains the fields at $ft = 2\pi$. The temperature is similar to the initial temperature, but there is a slight tilt and the maximum temperature gradient is shifted toward the warm air at the bottom and vice versa at the top. The velocity fields are weak at this time, but some small-scale features remain in the divergence and vorticity fields.

These results agree quite well with the theory of section 3, which predicts an inertial oscillation in the velocity fields with frontogenesis followed by frontolysis when the Rossby number is below the critical value. However, by $ft = 2\pi$, the isotherms are no longer straight and the divergence and vorticity fields are not zero and they contain small-scale features. An effective way to compare the analytic and numerical solutions is through the frontal ''scale,'' which is defined

$$d = \frac{L^{-1}\Delta\theta}{\left|\left(\frac{\partial\theta}{\partial x}\right)_D\right|_{\max}}, \tag{6.1}$$

where the subscript D indicates a dimensional quantity. A slightly different definition of d is used in section 5 to measure the scale of u. An expression for d is derived in the appendix from the analytic solution in section 3.

Figure 10 compares the analytic solution for d (dashed) with the numerical solution at the boundary (solid) out to $ft = 2\pi$. The frontogenesis does not begin until $ft = 0.8$ because the wind field must be built up first. In the analytic solution the frontal scale decreases to less than one-third of its original value at $ft = \pi$, and then it returns to the original value at $ft = 2\pi$. The numerical solution has similar behavior, but the minimum value of 0.8 is larger. This is caused by the bar-

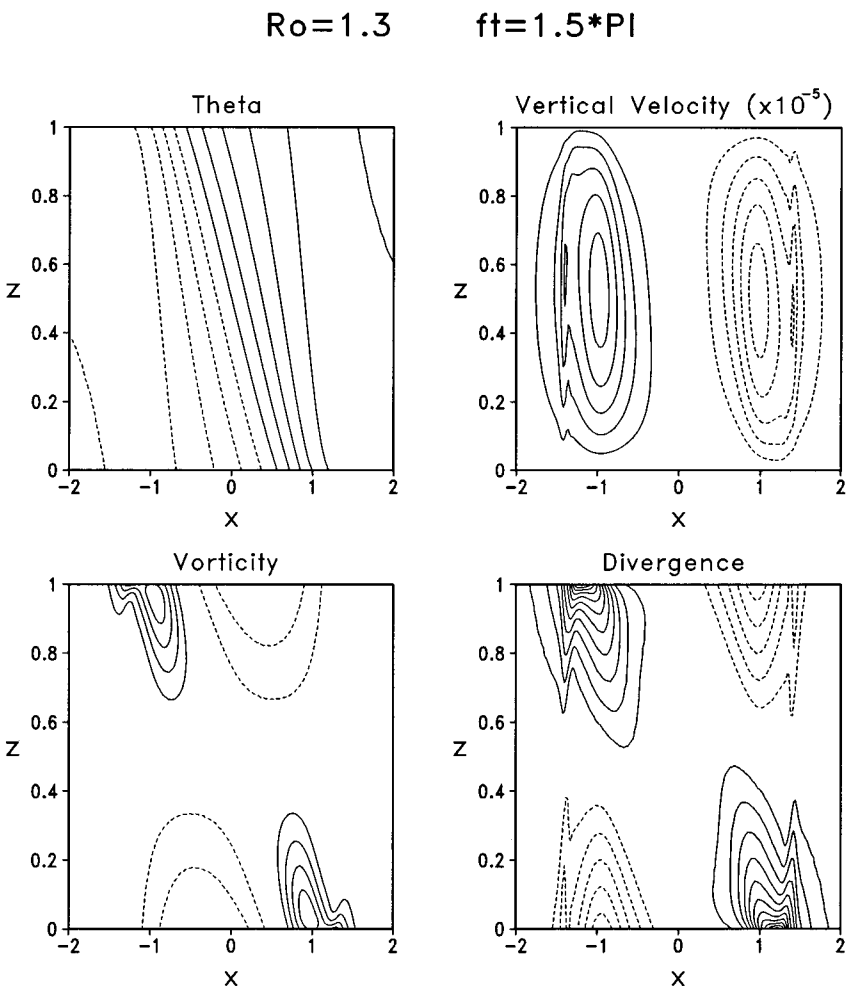

FIG. 8. For Ro = 1.3, the same fields and contour intervals as Fig. 6 but at $ft = 3\pi/2$. The extreme values of ζ and D are (0.58, −0.30) and (0.57, −0.33), respectively.

otropic pressure gradient term, which is not included in the analytic theory (see section 5). Also the numerical solution is not symmetric about $ft = \pi$. In particular the numerical solution for $ft > 5$ is less than the analytic solution. This may be related to the small-scale wind features that are seen at $ft = 3\pi/2$ (Fig. 8) and at $ft = 2\pi$ (Fig. 9).

Figure 11 compares the d values for three Rossby numbers at the lower boundary. The various curves represent: dotted (analytic solution), dashed (numerical solution with $\Delta x = 1/100$), and solid (numerical solution with $\Delta x = 1/50$). The minimum value for frontal formation in the analytic solution is Ro $= a_c = 1.435$. In this case the d value touches zero at $ft = \pi$ and then it increases to the initial value at $ft = 2\pi$. The numerical solutions only reach $d \simeq 0.4$ before increasing and, since the curves are very close the numerical truncation error, should be small. As expected from the analysis in section 5, the presence of the barotropic component of the pressure gradient force requires a larger Rossby number for the formation of a discontinuity.

For Ro = 1.55, the analtyic solution becomes discontinuous at $ft = 2.37$. The two numerical solutions suggest that d would go to zero if the grid size could be reduced to zero. It appears that the critical time for the corresponding frontal formation would be $ft = \pi$, which agrees with the time for discontinuity formation in the limiting analytic solution (Ro $= a_c$). This suggests that the minimum value for frontal formation for the complete system of equations is very close to Ro = 1.55. It is not possible to compute this value exactly by finite differences. It is reasonable to expect that the limiting case would occur at $ft = \pi$, because that is when the divergence field changes sign in the inertial oscillation.

For the case Ro = 1.8 the analytic d value drops rapidly to zero at $ft = 1.80$. The two numerical solutions are very close until d reaches 0.2. If we extrapolate from the $\Delta x = 1/100$ case the discontinuity would occur at about $ft = 2.4$. Note that as the forcing becomes stronger the analytic and numerical critical times come closer together. In this situation the barotropic pressure gra-

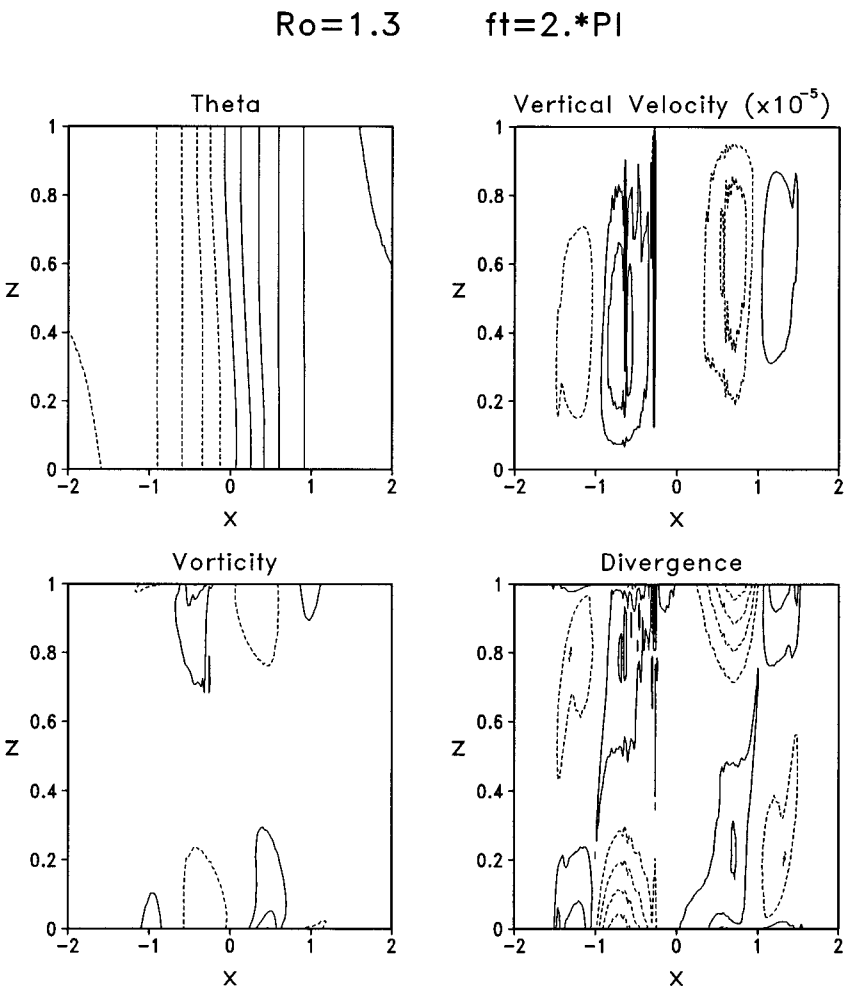

FIG. 9. For Ro = 1.3, the same fields and contour intervals as Fig. 6 but at $ft = 2\pi$.

dient terms are less important, as might be expected since the basic frontogenesis is stronger.

Figure 12 contains θ, w, vorticity, and divergence cross sections at $ft = 1.05$ for Ro = 1.8. This is a little less than half-way along the time evolution to a discontinuity. At this time the various fields are similar to those shown in Fig. 6 for the Ro = 1.3 fields at $ft = \pi/2$. Figure 13 contains the same fields at $ft = 2.1$, which is close to the estimated time of discontinuity formation on the boundaries. The temperature field is nearly discontinuous on both boundaries. Note that the maximum temperature gradient has propagated into the warm air at the lower boundary and into the cold air at the upper boundary, so that the frontal zone is clearly not a material surface. This general behavior is included in the theory of section 3 and is measured by the quantity $(ax_o)_m$ in the appendix. The convergence field is highly concentrated around the lower and upper fronts with weaker divergence, above and below, respectively. This leads to a strong jet in the vertical velocity above and below the frontal locations. The frontogenesis is caused by the strong convergence in the surface frontal zones. There is strong cyclonic vorticity extending inward from both boundary fronts. The large vorticity regions are wider than the convergence zones and they show only a slight tilt with height. Note the presence of spike-shaped isolines of vorticity, which show the strong advection of vorticity by the vertical jet. The structure of these fronts are different from the quasi-balanced fronts such as those studied by Hoskins and Bretherton (1972). This will be discussed further in section 7.

The time behavior of d for Ro = 1.8 is very similar to the behavior in the nonrotating cases where $d \to 0$ linearly because there is no opposing Coriolis effect. The analytic solution for d with $f = 0$ can be found in the appendix. In particular the time when $d = 0$ can be found by substituting $(ax_o)_m = 1/\sqrt{2}$ into (A.3) and then solving for t. When $f = 0$ the critical time becomes

$$t_0 = \frac{L}{V}(8\pi e)^{1/4}, \tag{6.2}$$

where $V = [g\Delta\theta h/\theta(o)]^{1/2}$. The critical time for $f \neq 0$ is

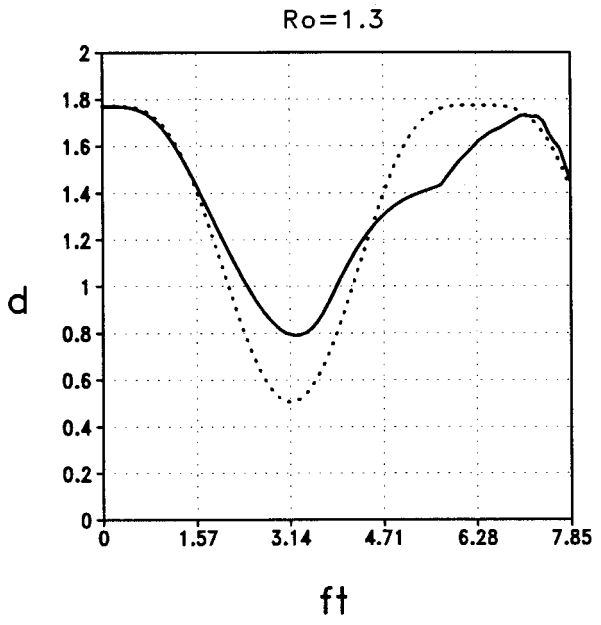

FIG. 10. The frontal scale d [defined by (6.1)] as a function of time for Ro = 1.3. The dotted line is for the analytic solution and the solid line is for the numerical solution.

$$t_f = \frac{2}{f}\arcsin\left[\frac{1}{\mathrm{Ro}}\left(\frac{e\pi}{2}\right)^{1/4}\right]. \tag{6.3}$$

If we take the ratio of these two times, we obtain

$$\frac{t_0}{t_f} = \frac{\left(\frac{e\pi}{2}\right)^{1/4}\mathrm{Ro}^{-1}}{\arcsin\left[\left(\frac{e\pi}{2}\right)^{1/4}\mathrm{Ro}^{-1}\right]}, \tag{6.4}$$

where we have used $\mathrm{Ro} = V/fL$. Note that the formula gives $t_f = t_o$ in the limit $\mathrm{Ro} \to \infty$ as expected. For Ro = 1.8 the ratio (6.4) is 0.863. This indicates that this case behaves in time similarly to the nonrotating case.

The expression for time of formation (6.2) in the nonrotating case can be written in terms of the initial temperature field by first putting (3.18) in dimensional form, which leads to

$$t_0 = \frac{2r}{\sqrt{\frac{gh}{\theta(0)}\left|\frac{\partial^2\theta}{\partial x^2}\right|_{\max}}}, \tag{6.5}$$

where r approximately represents the effects of the barotropic part of the pressure gradient. Our numerical integrations (not shown) indicate that $r \simeq 1.2$ for the error function initial condition. Equation (6.5) agrees with the expression in Simpson and Linden (1989) when it is corrected following Kay (1992).

The numerical solutions of this section generally agree with the theory of section 3. The critical Rossby number is increased by about 0.1 due to the presence of the barotropic part of the pressure gradient as expected from the results of section 5. For the frontogenesis cases, a strong, narrow jet is produced above the surface front. In the no front regime small-scale features develop that do not go to zero at the end of the inertial oscillation.

We have also carried out numerical integrations with the sinusoidal initial state that is employed by Blumen (2000). The numerical solutions are similar to those given in this section except the frontogenesis tends to produce a near spike on the boundaries rather than a nearly discontinuous jump. Our numerical solutions generally agree with Blumen's analtyic solutions except that the formation of the fronts is delayed and the critical Rossby number is increased, as in the current study. The solution structure near the discontinuity time also departs from the analytic solutions (e.g., its isotherms are no longer straight). In general, our conclusions about the importance of the barotropic pressure gradient term are the same as with the error function initial state.

7. Conclusions

The analytic theory described in section 3 is also given by Blumen (2000) with oceanographic applications. The theory uses momentum coordinates to obtain nonlinear solutions to a geostrophically unbalanced initial state with zero potential vorticity. When the initial Rossby number is below a critical value, which is of order 1, the horizontal wind components along the upper and lower boundaries display an inertial oscillation. During the first part of the inertial period ($0 < ft < \pi$), the temperature develops a tilt and frontogenesis begins, while in the second part of the period ($\pi < ft < 2\pi$) the isotherms return to a vertical orientation and frontolysis brings the temperature gradient back to its initial value at $ft = 2\pi$. When the initial Rossby number is equal to the critical value a discontinuity forms at $ft = \pi$. For larger values of the Rossby number a frontal discontinuity forms before $ft = \pi$.

The analytic theory is based on the neglect of the barotropic part of the pressure gradient. The importance of this term is investigated in a simple scale collapse problem with a constant potential temperature and no Coriolis force. It is found that the presence of the barotropic term opposes the formation of discontinuities.

Numerical simulations of the original problem with the error function initial temperature field show that the presence of the barotropic pressure gradient term delays frontogenesis, as expected. In particular, the critical Rossby number is increased from 1.435 to about 1.55. For Ro = 1.3 the numerical solution is generally similar to the analytic solution, but the frontal zones that develop are weaker and the isotherms do not remain straight as predicted by the theory (Blumen 2000). In addition some small-scale features in the divergence and vertical motion are present at $ft = 2\pi$, and the vorticity

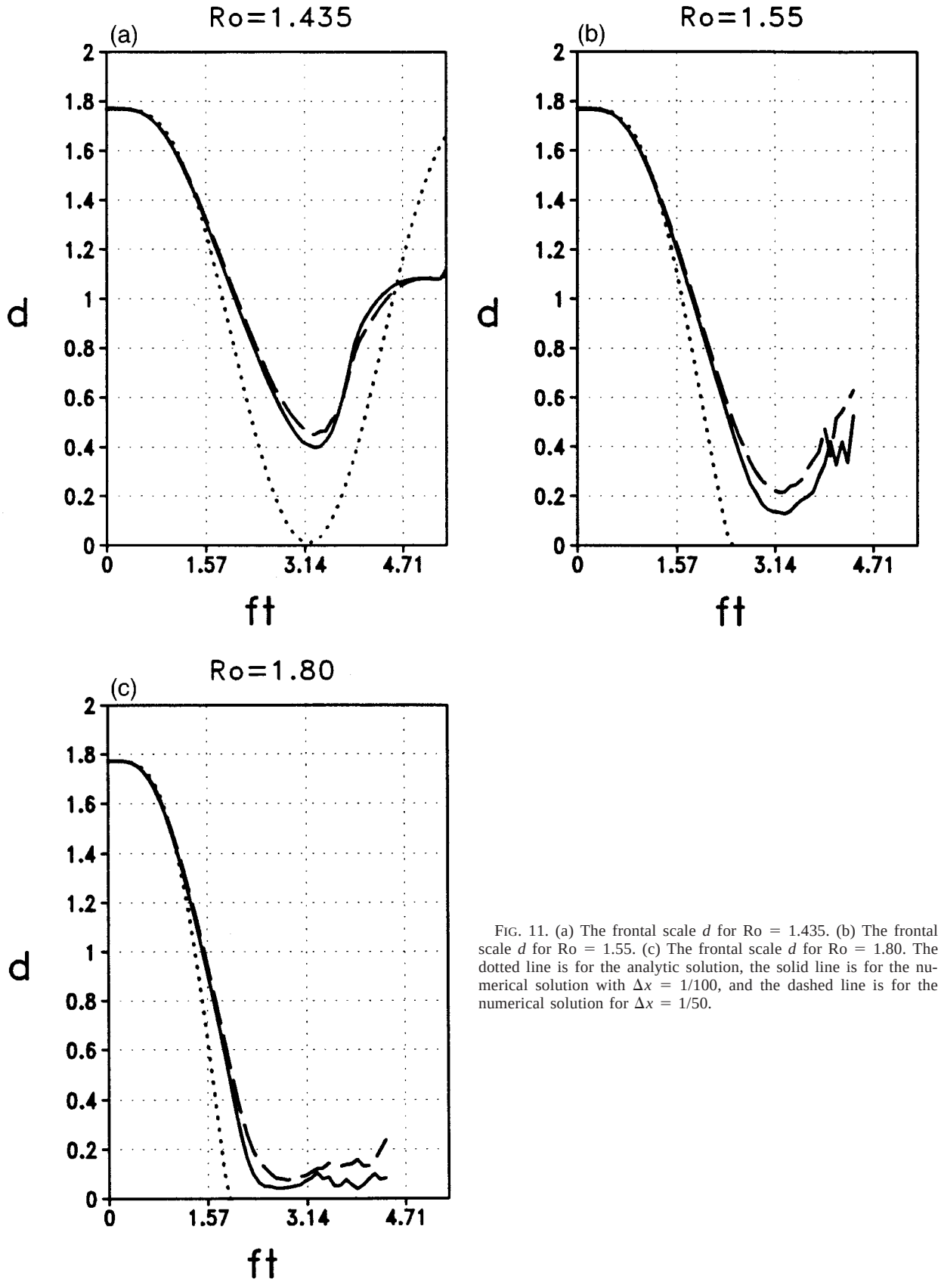

FIG. 11. (a) The frontal scale d for Ro = 1.435. (b) The frontal scale d for Ro = 1.55. (c) The frontal scale d for Ro = 1.80. The dotted line is for the analytic solution, the solid line is for the numerical solution with $\Delta x = 1/100$, and the dashed line is for the numerical solution for $\Delta x = 1/50$.

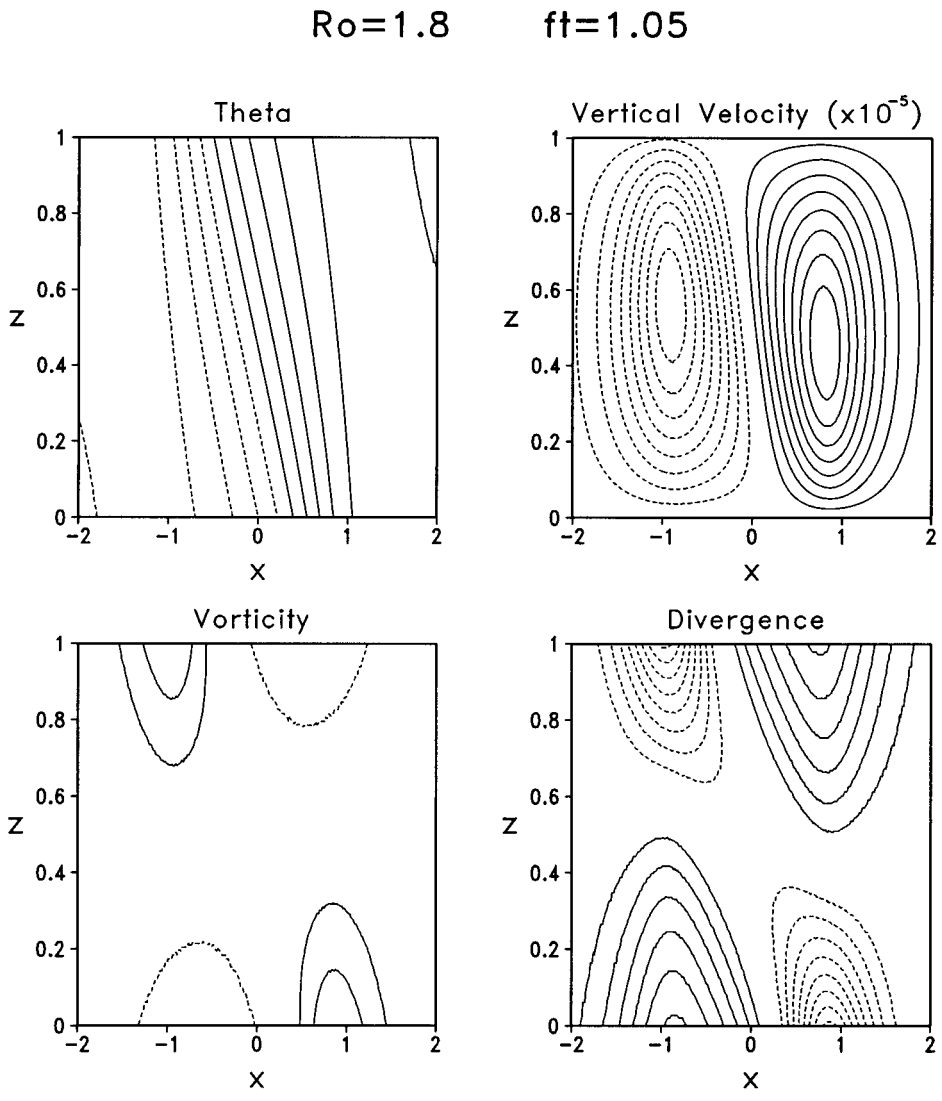

FIG. 12. For Ro = 1.8, the various fields at $ft = 1.05$. The same fields as in Fig. 6. The contour intervals are θ, 0.2; w, 10^{-5}; ζ, 0.1; D, 0.05. The extreme values for w, ζ, and d are (8.75, −8.75), (0.3, −0.16), and (0.31, −0.46), respectively.

field shows evidence of vertical advection by a small-scale jet. These differences from the analytic theory increase as the Rossby number increases, and as the discontinuity time is approached. For Ro = 1.8 the solutions are closer to the nonrotating solution where the frontal scale drops rapidly to zero. The analytic and numerical values for the frontogenesis time in the nonrotating case compare well with previous studies such as Simpson and Linden (1989) and Kay (1992).

The unbalanced frontogenesis problem with zero potential vorticity does not lead to steady-state solutions contrary to the expectations of Ou (1984) and Blumen and Wu (1995). When the Rossby number is less than the critical value, inertial oscillations occur since the internal gravity waves cannot carry energy away with zero static stability. When a front forms it is unlikely that a steady state would be achieved even if diffusive terms were included. In the frontal regions (near the upper and lower boundaries) the frontogenetic forcing will be approximately balanced by the diffusion terms, while away from the fronts the inertial oscillation would continue. This could lead to a small strengthening of the fronts until $t \sim \pi f^{-1}$ and weakening between πf^{-1} and $2\pi f^{-1}$. Although this behavior has not been demonstrated numerically, we believe that this type of front will have a short lifetime in comparison with balanced fronts. The latter have longer timescales and they can remain in an approximate steady state as long as the synoptic forcing continues (Williams 1974; Snyder et al. 1993). For example, Sanders (1999) analyzes a very short-lived cold front that appears to be the result of unbalanced frontogenesis.

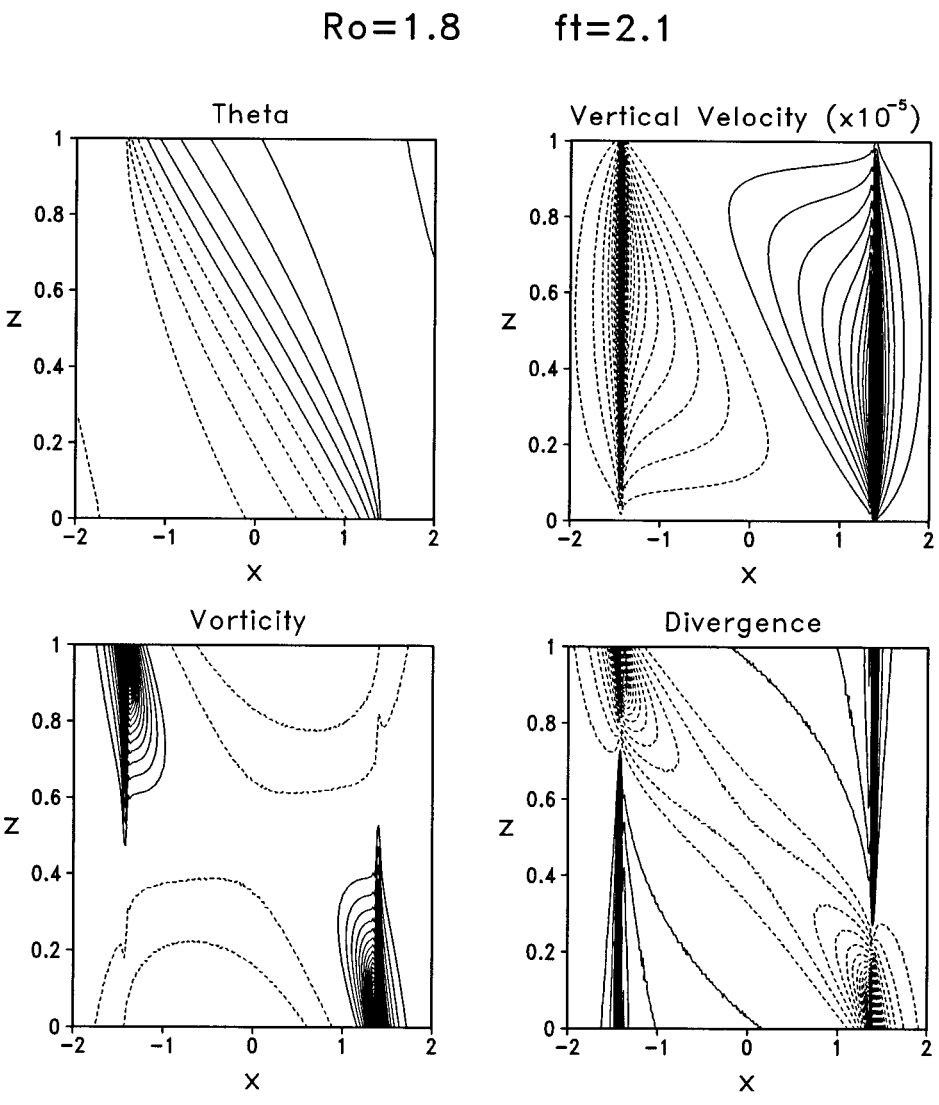

FIG. 13. For Ro = 1.8 the various fields at $ft = 2.1$. The same fields and contour intervals as in Fig. 12. The extreme values of w, ζ, and D are (35.4, −35.4), (7.20, −0.29), and (0.65 and −4.37), respectively.

Unbalanced fronts have large vorticity in the frontal zone and a stable tilt, but the thermal wind equation is not satisfied as it is in balanced fronts. In balanced frontogenesis the divergence is a nearly constant (small) percentage of the vorticity throughout the frontogenesis process. During the unbalanced frontogenesis discussed in this paper the divergence develops before the vorticity, but the latter then grows rapidly. In general the relation between the vorticity and the divergence varies considerably as the front evolves, in contrast to balanced frontogenesis. Also, we find that unbalanced fronts can propagate into the warm air at the lower levels and into the cold air in the upper levels. Thus, the air parcels do not tend to stay in the frontal zone as they do in a balanced front.

Unbalanced fronts in the atmosphere can be initiated by large heating gradients near the surface. For example, when low-level clouds are present behind a cold front, solar heating can induce unbalanced frontogenesis, which can greatly intensify the original cold front (Segal et al. 1986; Koch et al. 1995; Blumen et al. 1996). Our results demonstrate unbalanced frontogenesis, but the rigid upper lid is not very realistic. If this boundary were replaced by a stable layer, we would still expect surface frontogenesis that is similar to that found in this model. In particular, the narrow, strong vertical jet that occurs near frontogensis time could penetrate the stable layer and cause deep convection if there were conditionally unstable air above the stable layer. In this case, the ensuing frontal evolution would be controlled by moist cloud dynamics, and gravity wave propagation along the interface.

In Part II we will consider constant vorticity flows, which will begin with a constant static stability. This

will allow gravity waves to carry energy away from the initial imbalance or the frontal zone. In the current study this is not possible because the static stability is zero and inertial oscillations have zero group velocity. In Part II a critical curve will be obtained in terms of the Rossby number and the Froude number, which separates frontogenesis cases from nonfrontogenesis cases.

Acknowledgments. The research of RTW was supported in part by the National Science Foundation (NSF), Division of Atmospheric Science, under Grant ATM-9208751, and by the Naval Research Laboratory Program Element 0601153N, sponsored by the Office of Naval Research. The research of WB was supported in part by NSF Grants ATM-9627792 and ATM-9903645. The authors would like to thank Dr. M. S. Peng, Dr. B.-F. Jeng, Mrs. O. Haney, and LCDR Alberto Neves for their assistance with this research. Mrs. P. Jones carefully typed the manuscript. The authors would also like to thank Dr. S. Garner and an anonymous reviewer for their helpful comments on the manuscript.

APPENDIX

Calculation of *d* Variation from Analytic Solution

An effective way to compare the numerical solutions of section 6 with the analytic solution of section 3 is via the frontal scale *d*, which is defined by (6.1). The dimensional temperature gradient, which is required for (6.4) can be written:

$$\left(\frac{\partial\theta}{\partial x}\right)_D = \frac{\Delta\theta}{La}\frac{\partial\theta}{\partial x} = \frac{\Delta\theta}{La}\frac{\partial\theta_0}{\partial x_0}\frac{\partial x_0}{\partial x} = \frac{\Delta\theta}{La}\frac{\partial\theta_0}{\partial x_0}\frac{1}{1-\dfrac{\partial v}{\partial x_0}}, \quad \text{(A.1)}$$

where the last step comes from the transformation to momentum coordinates. With (2.15), (3.4), and (3.13) this equation can be rewritten as follows:

$$\left(\frac{\partial\Theta}{\partial x}\right)_D = \frac{\Delta\theta L^{-1}\pi^{-1/2}e^{-(ax_0)^2}}{1-\dfrac{4}{\pi^{1/2}}\left(\dfrac{g\Delta\theta h}{\theta(0)L^2}\right)\left(\dfrac{1}{2}-z\right)\dfrac{\sin^2(ft/2)}{f^2}ax_0e^{-(ax_0)^2}}. \quad \text{(A.2)}$$

To find the maximum temperature gradient we differentiate (A.2) with respect to ax_o and equate the result to zero, which gives

$$(ax_0)_m = \frac{2}{\pi^{1/2}}\frac{g\Delta\theta h}{\theta(0)L^2}\left(\frac{1}{2}-z\right)\frac{\sin^2(ft/2)}{f^2}e^{-(ax_0)_m^2}. \quad \text{(A.3)}$$

This equation is solved iteratively for $(ax_o)_m$ beginning with $(ax)_m = 0$ for $t = 0$. As time is increased each iteration begins with the $(ax_o)_m$ from the previous time.

The final expression for *d* is obtained by substituting (A.3) into (A.2) and then inserting the result into (6.1):

$$d = \frac{1-2(ax_0)_m^2}{\pi^{-1/2}e^{-(ax_0)_m^2}}. \quad \text{(A.4)}$$

Inspection of (A.4) shows that $(ax_o)_m = 1/\sqrt{2}$ when the discontinuity forms. The nonrotating case can be included by letting *f* go to zero in (A.3). This formula can be applied at $z = 0$ and $z = h$ where the gradients are largest.

REFERENCES

Blumen, W., 2000: Inertial oscillations and frontogenesis in a zero potential vorticity model. *J. Phys. Oceanogr.,* **30,** 31–39.

——, and R. Wu, 1995: Geostrophic adjustment: Frontogenesis and energy conversion. *J. Phys. Oceanogr.,* **25,** 428–438.

——, N. Gamage, R. L. Grossman, M. A. LeMone, and L. J. Miller, 1996: The low-level structure and evolution of a dry arctic cold front over the central United States. Part II: Comparison with theory. *Mon. Wea. Rev.,* **124,** 1676–1692.

Estoque, M. A., 1962: The sea breeze as a function of the prevailing synoptic situation. *J. Atmos. Sci.,* **19,** 244–250.

Gall, R. L., R. T. Williams, and T. L. Clark, 1987: On the minimum scale of surface fronts. *J. Atmos. Sci.,* **44,** 2562–2674.

——,——, and ——, 1988: Gravity waves generated during frontogenesis. *J. Atmos. Sci.,* **45,** 2204–2219.

Hoskins, B. J., and F. P. Bretherton, 1972: Atmospheric frontogenesis models: Mathematical formulation and solutions. *J. Atmos. Sci.,* **29,** 11–27.

——, and I. Draghici, 1977: The forcing of ageostrophic motion according to the semi-geostrophic equations and in an isentropic coordinate model. *J. Atmos. Sci.,* **34,** 1859–1867.

Jacqmin, D., 1991: Frontogenesis driven by horizontally quadratic distributions of density. *J. Fluid Mech.,* **228,** 1–24.

Kay, A., 1992: Frontogenesis in gravity-driven flows with non-uniform density gradients. *J. Fluid Mech.,* **235,** 529–556.

Koch, S. E., J. McQueen, and V. M. Karyampudi, 1995: A numerical study of the effects of differential cloud cover on cold front structure and dynamics. *J. Atmos. Sci.,* **52,** 937–964.

Ou, H. W., 1984: Geostrophic adjustment: A mechanism for frontogenesis. *J. Phys. Oceanogr.,* **14,** 994–1000.

Sanders, F., 1999: A short-lived cold front in the southwestern United States. *Mon. Wea. Rev.,* **127,** 2395–2403.

Segal, M., F. W. Purdon, J. L. Song, R. A. Pielke, and Y. Mahrer, 1986: Evaluation of cloud shading effects on the generation and modification of mesoscale circulations. *Mon. Wea. Rev.,* **114,** 1201–1212.

——, W. L. Physick, J. E. Heim, and R. W. Arritt, 1993: The enhancement of cold front temperature contrast by differential cloud cover. *Mon. Wea. Rev.,* **121,** 867–873.

Simpson, J. E., and P. F. Linden, 1989: Frontogenesis in fluid with horizontal density gradients. *J. Fluid Mech.,* **202,** 1–16.

Snyder, C., W. C. Skamarock, and R. Rotummo, 1993: Frontal dynamics near and following frontal collapse. *J. Atmos. Sci.,* **50,** 3194–3212.

Williams, R. T., 1974: Numerical simulation of steady state fronts. *J. Atmos. Sci.,* **31,** 1286–1296.

——, M. S. Peng, and D. A. Zankofski, 1992: Effects of topography on fronts. *J. Atmos. Sci.,* **49,** 287–305.

Wu, R., and W. Blumen, 1995: Geostrophic adjustment of zero potential vorticity flow initiated by a mass imbalance. *J. Phys. Oceanogr.,* **25,** 439–445.